Synergistically electronic interacted PVDF/CdS/TiO$_2$ organic-inorganic photocatalytic membrane for multi-field driven panel wastewater purification

Wei Li [a,*], Guocheng Liao [a], Wen Duan [a], Fanfan Gao [a], Yusen Wang [a], Rongxia Cui [a], Xuechuan Wang [b], Chuanyi Wang [c,*]

[a] College of Chemistry and Chemical Engineering, Shaanxi Key Laboratory of Chemical Additives for Industry, Shaanxi University of Science and Technology, Xi'an, Shaanxi 710021, China
[b] College of Bioresources Chemical and Materials Engineering, Shaanxi University of Science & Technology, Xi'an, Shaanxi 710021, China
[c] School of Environmental Sciences and Engineering, Shaanxi University of Science and Technology, Xi'an, Shaanxi 710021, China

ABSTRACT

Solar-driven wastewater purification technology is a promising candidate to solve the hazards of water contaminants. However, it is difficult for most of particulate photocatalysts to maintain durable photoactivity due to its micro/nano size. Herein, a synergistically electronic interacted membrane catalyst with large extending area and high pollutant capture capacity was processed based on a highly active CdS/TiO$_2$ heterojunction and ferroelectric polyvinylidene fluoride for achieving highly efficient Cr^{6+}-to-Cr^{3+} (CTC) reduction (1.6×10^{-2} min^{-1}) and synchronous decomposition of organic matters (methylene blue (1.2×10^{-2} min^{-1}) and bisphenol A (0.6×10^{-2} min^{-1})) under simulated sunlight (SSL, 74.1 mW·cm^{-2}) irradiation following a durably steady photoactivity even being recycled for 20 times, which effectively avoided the hazards of secondary pollution. Subsequently, a tailor-made panel wastewater purification system was first built based on this membrane catalyst to drive CTC reduction and synchronous organic matter degradation, and high-efficiency purification performance was presented on this panel system under multi-field drive of light-activation and piezoelectric polarization. This work provides an insight for photocatalytic wastewater purification through membrane catalyst assisted panel technology.

1. Introduction

Industrial and agricultural production processes usually produce a large amounts of wastewater containing unfriendly matters (e.g. organic matters and heavy metal ions) [1,2], which will inevitably pose a great threat to ecosystem. Hexavalent chromium (Cr^{6+}), a Class A carcinogen listed by WHO International Agency of Research on Cancer [3], is mainly produced in the fields of electroplating, wool dyeing and finishing, leather tanning, anti-corrosion, coating production, etc [4,5]. Therefore, solving Cr^{6+} wastewater pollution is related to people's livelihood and safety, and is in line with the strategic purpose of green sustainable development. Trivalent chromium (Cr^{3+}) is a beneficial heavy metal ion to organisms [6], so Cr^{6+}-to-Cr^{3+} (CTC) reduction can effectively address the hazards of Cr^{6+} wastewater [7]. However, it should be noted that Cr^{3+} is easily complexed with organic matters in

water system to form organic chromium complex, and it will also lead to allergic symptoms to human body in case of excess [8]. Generally, chromium-containing wastewater (CCW) contains abundant organic matters, thereby the secondary harms of organic chromium should also be paid attention while solving Cr^{6+} pollution.

Solar-driven photocatalysis technology, has attracted much attention in environmental and energy fields, is identified as a promising candidate to relieve the hazards of wastewater due to the merits of simple operation, sustainability, low cost, etc [9,10]. Under photo-activation, the generated reductive/oxidizing excitons (e$^-$ and h$^+$) and radicals (•O$_2^-$ and •OH) can easily achieve aqueous CTC reduction [11,12] and synchronous decomposition of organic matters [13,14] to completely eliminate the hazards of CCW. However, conventional photocatalysts are mostly micro/nano-sized semiconductor materials [15–17], which is difficult to maintain a stable microstructure and steady photoactivity

under long-term photo-activation. Immobilizing micro/nano particulate catalyst on large-sized matrix (e.g. SiO_2 [18], Al_2O_3 [19], carbon material [20], etc.) is a customary means to improve its operability and stability. However, photocatalytic process is highly dependent on the light absorption, so it requires the catalyst to have a large extending area for fully harvesting photon energy, which has greatly promoted the development of two-dimensional (2D) photocatalytic materials. In recent years, the panel reaction technology has been getting more and more attention. For example, Prof. Domen et al. developed a $100\,m^2$-scale panel system based on Al-doped particulate $SrTiO_3$ photocatalyst for solar-to-hydrogen (STH) conversion [21], and Mi et al. also reported a panel system based on particulate InGaN photocatalyst for water-splitting [22]. Obviously, the current photocatalytic panel system is mainly devoted to achieve water splitting to hydrogen production, and its application in wastewater purification has been rarely reported.

Owing to the inherent merits of the panel photoreaction technique, we first proposed its application in wastewater purification. Herein, a synergistically electronic interacted membrane catalyst with large extending area and high pollutant capture capacity was processed based on a highly active CdS/TiO_2 heterojunction and ferroelectric poly-vinylidene fluoride (PVDF) for CCW purification under simulated sunlight (SSL) irradiation. Owing to the unique merits of adjustable dimension, high extending area, good flexibility and convenient operability, etc., efficient and steady CTC reduction and synchronous decomposition of organic matters (methylene blue (MB) and bisphenol A (BPA)) were achieved by this membrane catalyst, which effectively avoided the hazards of secondary pollution. Subsequently, a tailor-made membrane catalyst assisted panel wastewater purification system was built to progress the CTC reduction and synchronous organic matter degradation, and high-efficiency purification performance was presented on this panel system under multi-field drive of light-activation and piezoelectric polarization. This work provides an insight for photocatalytic wastewater purification through membrane catalyst assisted panel technology.

2. Experimental section

The reagents illustration, synthetic methods of TiO_2 NPs and CdS NRs, characterizations, parameters for photoelectric property tests and calculation method of band gap are provided in Supplementary Material.

2.1. Preparation of CdS/TiO2 composite photocatalyst

The TiO_2 NPs and CdS NRs were synthesized by following our previous methodologies [23,24], and the detailed operations are provided in Supplementary Material. Subsequently, the CdS/TiO_2 composite photocatalyst was solvothermally prepared by introducing as-synthesized TiO_2 NPs into the precursor system of CdS NRs (Fig. 1).

Specifically, $0.047\,g$ TiO_2 NPs was ultrasonically dispersed in $80\,mL$ EDA dissolving $2.85\,g$ CH_4N_2S and $2.955\,g$ $Cd(Ac)_2 \cdot 2\,H_2O$ to form a uniform mixture under $40\,min$ of magnetic agitation following a $100\,mL$ closed autoclave reaction for $24\,h$ at $160\,°C$. After the reaction, the product was centrifuged and rinsed several times with deionized water to gain a yellow powdered $CdS/TiO_{2(x\%)}$ composite catalyst after drying at $60\,°C$ for $12\,h$. Here, x% represents the percentage of TiO_2 NPs in composite catalyst, where x = 15, 17.5, 20, 22.5, 25, respectively.

2.2. Processing of PVDF/CT organic-inorganic membrane

The electrospinning technique was adopted to process the PVDF/CT organic-inorganic membrane by compounding optimal CdS/TiO_2 composite photocatalyst with PVDF (Fig. 1). Concretely, $0.5\,g$ PVDF powder ($\overline{M} = 500$ thousands) was dissolved in the mixed solvent of $3.36\,mL$ DMF and $2.24\,mL$ acetone, and a certain amount of optimal CdS/TiO_2 composite photocatalyst was ultrasonically dispersed in this polymer solution. The precursor mixture for electrospinning was obtained by continuous stirring for $30\,min$ at $40\,°C$, which was transferred to a $10\,mL$ syringe and sprayed at a steady flow rate of $1\,mL\bullet h^{-1}$ and potential of $9.32\,kV$ through a $0.66\,mm$ needle. Rotating speed of collecting drum was $200\,rpm$, which is $15\,cm$ from the needle, and the moving speed of sliding platform was $32\,mm\bullet s^{-1}$. After spinning, the PVDF/CT organic-inorganic membrane with a size of $21\,cm \times 24\,cm$ was obtained and dried for $2\,h$ at $60\,°C$. Similarly, a series of organic-inorganic membranes were processed by adjusting the amount of inorganic catalyst, and the resultant membrane materials were expressed as PVDF/CT$_{y\%}$, where y% represents the percentage of inorganic catalyst in composite membranes. Meanwhile, pristine PVDF membrane was also processed for contrast by the same procedure at absence of inorganic photocatalyst.

2.3. SSL-driven CCW purification

Firstly, $K_2Cr_2O_7$ aqueous solution was used to simulate Cr^{6+} wastewater to assess the CTC reduction capacities of the catalysts under SSL-irradiation. Specifically, $50\,mg$ inorganic catalyst was ultrasonically dispersed in $50\,mL$ $0.2\,mM$ $K_2Cr_2O_7$ aqueous solution to continuously agitate for $1\,h$ in dark. A mild xenon lamp (BBZM-I, $74.1\,mW\cdot cm^{-2}$, CN, Fig. 3(a)) was used to simulate the sunlight to irradiate the aqueous dispersion, and DPC method was adopted periodically to determine Cr^{6+} concentration in solution.

Generally, Cr^{6+}, Cr^{3+} and organic matters coexist in actual CCW, so common organic matters (e.g. MB and bisphenol A (BPA), etc.) were added to $K_2Cr_2O_7$ solution to simulate the actual industrial CCW environment, so as to assess the comprehensive CCW purification capacity of optimal catalyst. Specifically, $50\,mg$ optimal inorganic catalyst was ultrasonically dispersed in $50\,mL$ $0.2\,mM$ $K_2Cr_2O_7$ solution containing $10\,mg/L$ organic matters to continuously agitate for $1\,h$ in dark. Same light source was used to irradiate the aqueous dispersion, and regularly extracting the solution to determine the concentration of organic
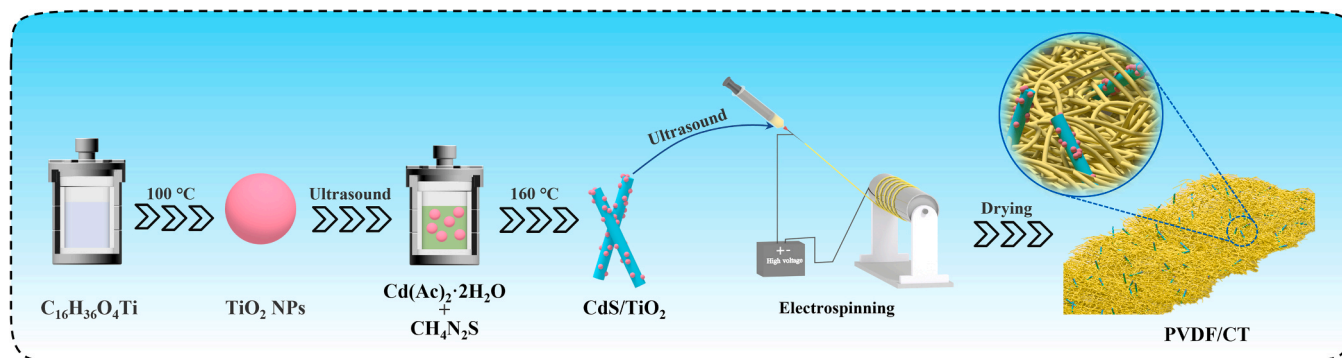

Fig. 1. Preparation diagram of CdS/TiO2 composite photocatalyst and PVDF/CT membrane catalyst.

matters and Cr^{6+} ions, so as to assess the CTC reduction capacities and synchronous decomposition of organic matters on the optimal inorganic catalyst. In order to determine the actual mineralization ability of the catalyst to organic matters, total organic carbon (TOC) content of the solution during the purifying process was recorded on a TOC analyzer (VARIO, Elementar, Germany).

For membrane catalysts, a circular membrane catalyst with a diameter of 10 cm was cut to replace inorganic catalyst and fixed in a fixator to drive CCW purification in a petri dish with an optical quartz glass cover, and membrane catalyst was impregnated 0.5 cm below the liquid level in all irradiating process. After the reaction, membrane catalyst

was collected and rinsed several times with deionized water, and regeneration was achieved after soaking in dilute hydrochloric acid solution (pH = 2.0) for 1 h. All cyclic experiments were performed using the same procedure.

The error bars of each data were determined through three measurements.

2.4. Photoelectric property tests

All photoelectric data was detected on an electrochemical workstation (CHI 660E, CN) equipped a 350 W xenon lamp (Fig. 3(a)). A three-
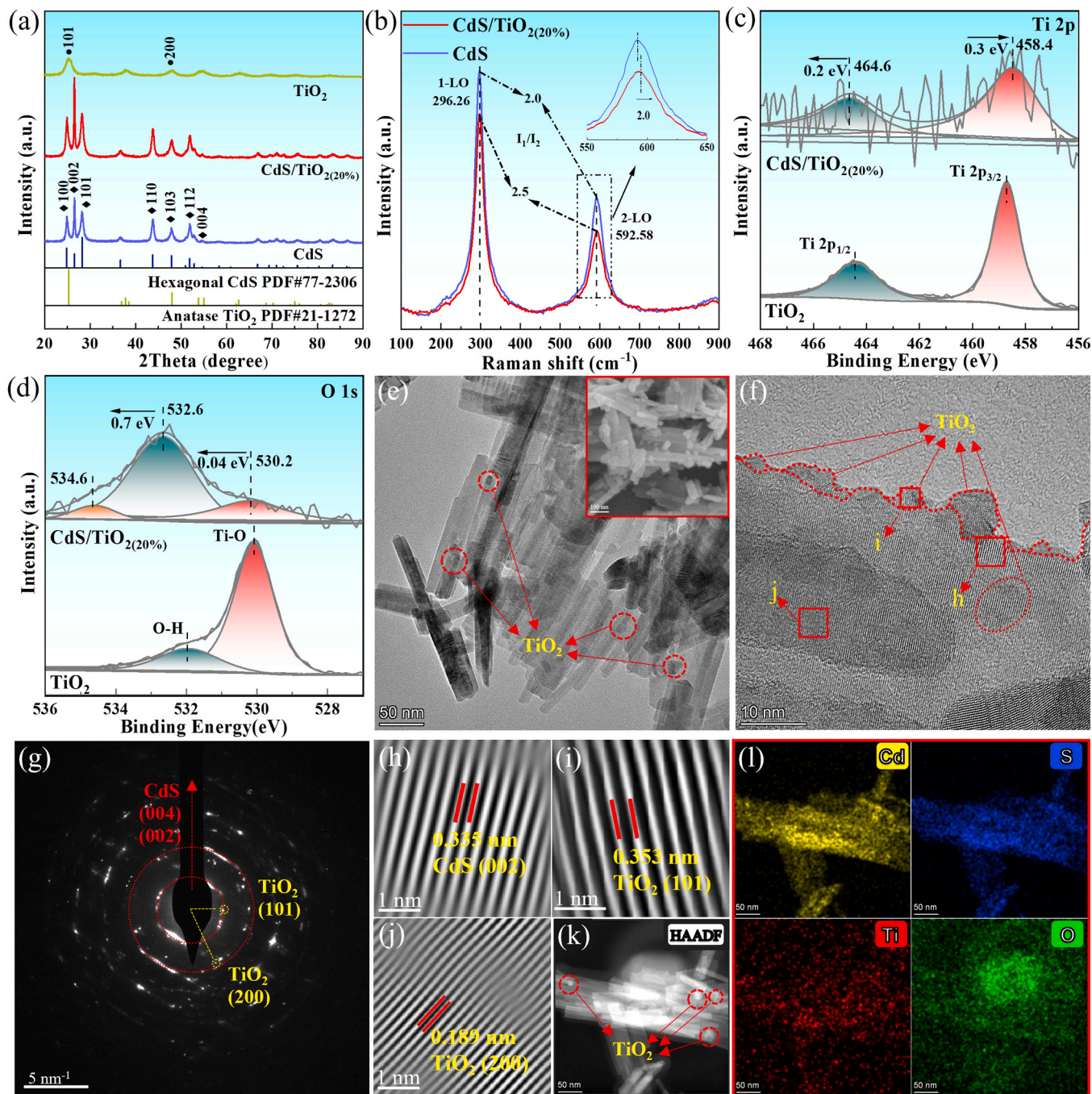

Fig. 2. (a) XRD patterns of bare CdS NRs, TiO$_2$ NPs and CdS/TiO$_{2(20\%)}$ composite catalyst. (b) Raman spectra of bare CdS NRs and CdS/TiO$_{2(20\%)}$ composite catalyst. High-resolution XPS spectra of bare TiO$_2$ NPs and CdS/TiO$_{2(20\%)}$ composite catalyst: (c) Ti 2p and (d) O 1 s core-levels. (e) TEM, (f) HRTEM images, (g) SAED pattern, (k) HAADF image and (l) EDX mappings of CdS/TiO$_{2(20\%)}$ composite catalyst. (h-j) Partial magnifications of panel (f). Inset of panel (e) is the corresponding SEM image.

electrode test system composed of working electrode, counter electrode (Pt electrode) and reference electrode (Ag^+/AgCl electrode) was installed in a quartz groove containing 0.2 M Na_2SO_4 electrolyte. For inorganic particulate catalysts, ITO glasses (15 mm × 15 mm) coated by tested samples were used as working electrodes. For membrane catalysts, 15 mm × 15 mm of copper conductive adhesive assisted square membranes were used as working electrodes. The specific operating parameters for each test item are provided in Supplementary Material.

3. Results and discussion

Appropriate amount of TiO_2 NPs was ultrasonically dispersed in the synthetic precursors of CdS NRs to prepare CdS/TiO_2 composite photocatalyst with highly dispersed TiO_2 NPs in bulk phase and surface at 160 ºC via a solvothermal method (Fig. 1). Regulation of TiO_2 content results in different dispersive states in composite, obtaining a series of CdS/TiO_2 composite photocatalysts with different contents of TiO_2. Subsequently, $K_2Cr_2O_7$ aqueous solution was used to simulate Cr^{6+} wastewater, and a mild xenon lamp (Fig. 3(a)) was used to simulate sunlight to assess the CTC reduction capacity of the catalysts, and the CdS/$TiO_{2(20\%)}$ composite was identified as the optimal catalyst (Fig. 3 (b,c)). Therefore, the microstructure and topology of this inorganic catalyst were investigated by essential characterizations.

3.1. Microstructure and topology of inorganic catalyst

The X-ray diffraction (XRD) patterns in Fig. 2(a) indicate that bare TiO_2 NPs and CdS NRs belong to typical anatase TiO_2 (PDF#21–1272) [25] and hexagonal CdS (PDF#77–2306) [26], and no hybrid peaks are observed, indicating that no impurity crystal phases are formed. However, the XRD pattern of CdS/$TiO_{2(20\%)}$ composite catalyst only shows strong diffraction peaks of hexagonal CdS, and no diffraction peaks corresponding to anatase TiO_2 can be observed, which ascribes to weak diffraction intensity and good dispersion of low content of TiO_2 NPs in CdS structure. Notably, the diffraction peaks of CdS/$TiO_{2(20\%)}$ composite catalyst at 2θ = 24.8°, 26.50° and 28.2° show significantly enhanced intensity compared with CdS NRs, which can be attributed to the crystal plane coupling between TiO_2 and CdS [27]. Raman spectrum in Fig. 2(b) shows representative characteristic peaks assigned to the first-order longitudinal optical (1-LO) mode and second-order longitudinal optical (2-LO) mode of hexagonal CdS at Raman shifts of 295 cm^{-1} and 592 cm^{-1} [28]. The peak intensity ratio of 1-LO and 2-LO appears obviously increase (I_1/I_2 = 2.5) compared with CdS NRs (I_1/I_2 = 2.0), and 2 nm of peak redshift can be observed from the partial magnification (550–650 cm^{-1}) of 2-LO mode, which ascribes to the electronic interaction at TiO_2/CdS heterointerface [29]. X-ray photoelectron spectroscopy (XPS) was performed to determine the electronic interaction at TiO_2/CdS heterointerface. High-resolution Ti 2p spectrum in Fig. 2(c) shows two weak peaks assigned to the Ti $2p_{1/2}$ and Ti $2p_{3/2}$ electron orbitals of Ti^{4+} at binding energies of 464.6 eV and 458.4 eV [30]. Two peaks (530.2 eV and 532.6 eV) in high-resolution O 1 s spectrum of Fig. 2(d) are assigned to the Ti-O bonds and surface O-H bonds [31], while the peak at binding energy of 534.6 eV ascribes to Cd-O-Ti bonding interaction at heterointerface [32]. Moreover, compared with bare CdS NRs and TiO_2 NPs, all peaks assigned to Cd 3d (Fig. S1(b)), S 2p (Fig. S1(c)) and O 1 s chemical states of CdS/$TiO_{2(20\%)}$ composite catalyst show slight shifts to higher binding energy direction following increased and decreased peak areas in different varying degrees. It demonstrates that TiO_2 NPs and CdS NRs successfully create the electronic interaction at heterointerface due to the formation of Ti-S and Cd-O chemical bonds, indicating the formation of synergetic heterojunction.

Transmission electron microscopy (TEM) and scanning electron microscopy (SEM) images in Fig. S2(a) indicate that bare CdS NRs appear typical nanorod morphology with smooth surface, while CdS/$TiO_{2(20\%)}$ composite photocatalyst show a rough surface with uniformly distributed nano-scale gibbosities (Fig. 2(e,f,k)). energy dispersion X-ray (EDX) mappings of Fig. 2(l) indicate that excepting the Cd, S and O elements, weak Ti element distribution can be observed in sample area, which is consistent with XPS survey spectrum in Fig. S1(a). The corresponding selected area electron diffraction (SAED) in Fig. 2(g) is significantly different from that of CdS NRs (Fig. S2(b)), and the diffractions assigned to (101) and (200) crystal planes of anatase TiO_2 can be observed except the diffraction rings of hexagonal CdS [33,34]. Moreover, excepting the lattice fringes (d = 0.335 nm) of (002) crystal plane of hexagonal CdS in nanorod region (Fig. 2(h)) [35], the lattice fringes (d = 0.353 nm and 0.189 nm) assigned to (101) and (200) crystal planes of anatase TiO_2[36,37] can be clearly observed from the partial magnified high-resolution TEM (HRTEM) images of Fig. 2(i,j). Therefore, the nano-scale gibbosities in sample area can be determined as TiO_2 NPs, and heterointerface between two components is clearly visible. This structure extremely benefits to the formation of synergistic electronic interaction at CdS/TiO_2 heterointerface.

3.2. CCW purification performance and photostability of inorganic catalyst

As shown in Fig. 3(b,c), TiO_2 NPs shows superior adsorption (12.7%) to Cr^{6+} ions in aqueous solution due to the good surface affinity, but very limited CTC reduction capacity was appeared under SSL-irradiation. Notably, CdS NRs has a low surface affinity to Cr^{6+} ions following a remarkable CTC reduction capacity, and about 96.6% of Cr^{6+} ions was reduced during 40 min of SSL-irradiation. Comparatively, all CdS/TiO_2 composite photocatalysts show enhanced Cr^{6+} adsorption/reduction capacity compared with bare TiO_2 NPs and CdS NRs, which is attributed to the strong Cr^{6+} affinity of TiO_2 NPs exposed on the surface and synergistic effect of CdS/TiO_2 heterointerface. Among which, about 9.8% (in dark, Fig. 3(b)) of saturated Cr^{6+} adsorption and highest CTC reduction rate (0.26 min^{-1} in 15 min of irradiation, Fig. 3(c)) were achieved on CdS/$TiO_{2(20\%)}$ composite photocatalyst, thereby it was determined as the optimal catalyst, and its CTC reduction rate is about 3.25-fold greater of CdS NRs (0.08 min^{-1}) and 13-fold greater of TiO_2 NPs (0.02 min^{-1}), respectively. High-resolution Cr 2p XPS spectrum in Fig. 3(i) demonstrates the successful CTC reduction due to the typical peaks assigned to Cr $2p_{1/2}$ and Cr $2p_{3/2}$ electron orbitals of Cr^{3+} at binding energies of 587.4 eV and 577.8 eV [8]. Moreover, both less and excess TiO_2 NPs in CdS/TiO_2 composite lead to decreased CTC reduction capacity. The former results in the insufficient formation of synergetic CdS/TiO_2 heterointerface, and the latter results in the damaged electronic interaction at CdS/TiO_2 heterointerface due to the aggregation of excessive TiO_2 NPs in CdS structure [38].

In general, Cr^{6+}, Cr^{3+} and organic matters coexist in actual CCW, of which Cr^{3+} ions easily coordinate with organic matters to form organic chromium with secondary hazards [8]. MB is a classic organic phenothiazine salt often contained in printing and dyeing wastewater [39], thereby 10 mg/L MB was added to 0.4 mM Cr^{6+} aqueous solution to assess the comprehensive CCW purification capacity of CdS/$TiO_{2(20\%)}$ composite photocatalyst by synchronously reducing Cr^{6+} ions and decomposing MB molecules. As shown in Fig. 3(d), MB addition did not show obvious impact on CTC reduction, and it was synchronously decomposed during 75 min of irradiation to achieve a 0.05 min^{-1} of degradation rate following a significant total organic carbon (TOC) decrease (Fig. S3(c)). Moreover, other organic matters (e.g. Rhodamine B, methyl orange, acid fuchsin) were also added to Cr^{6+} aqueous solution to investigate the comprehensive CCW purification capacity (Fig. S3 (a-f)), and satisfactory results were still maintained by this CdS/$TiO_{2(20\%)}$ composite photocatalyst. It indicates that the CTC reduction and synchronous decomposition of organic matters can be successfully achieved by this CdS/$TiO_{2(20\%)}$ composite photocatalyst under SSL-irradiation. EPR spectra in Fig. 3(f) indicates that the CdS/$TiO_{2(20\%)}$ composite photocatalyst can successfully generate superoxide ($\bullet O_2^-$) radicals under light-irradiation, while it is difficult to observe the signals
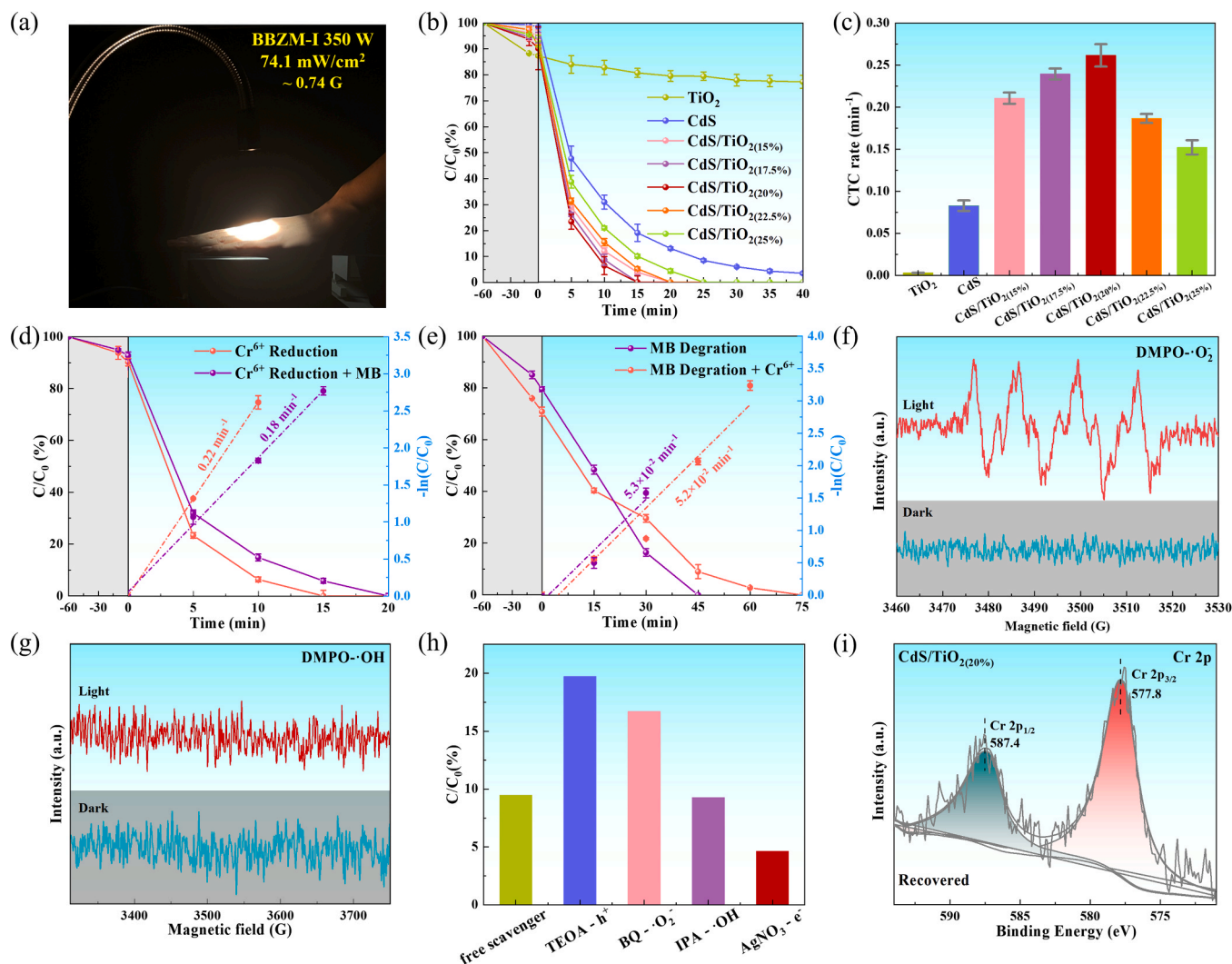
Fig. 3. (a) Digital photo of light source used in performance evaluation (Light density is about 74.1 mW·cm^{-2}). (b,c) CTC reduction capacities on CdS/TiO$_2$ composite photocatalysts with different contents of TiO$_2$ NPs. Comprehensive performance of CTC reduction (d) and synchronous MB decomposition (e) on CdS/TiO$_{2(20\%)}$ composite photocatalyst. EPR spectra of CdS/TiO$_{2(20\%)}$ composite photocatalyst at addition of DMPO in CH$_3$OH (f) and deionized water (g). (h) MB degradation performance of CdS/TiO$_{2(20\%)}$ composite photocatalyst at addition of different scavengers (p-benzoquinone (•O$_2$), isopropanol (·OH), AgNO$_3$ (e$^-$), triethanolamine (h$^+$)). (i) High-resolution Cr 2p XPS spectrum of recovered CdS/TiO$_{2(20\%)}$ composite photocatalyst. Error bars of panels (b-e) were determined through three measurements.

of hydroxyl (·OH) radicals (Fig. 3(g)). It indicates that the decomposition of organic matters mainly depends on the redox effect of photo-generated holes (h$^+$) and •O$_2$ radicals, and the results of radical trapping experiments in Fig. 3(h) support this conclusion well.

3.3. Photoelectric properties and exciton dynamics of inorganic catalyst

Optical and photoelectric properties are internal factors to determine the activity of photocatalytic materials. As is known to all, photocatalyst can no longer be regarded as a static system after being photo-activated, but belongs to a typical dynamic system, thereby all electrical properties in this study were measured under photoirradiation. UV-Vis absorption spectra in Fig. 4(e) shows that CdS/TiO$_{2(20\%)}$ composite photocatalyst possesses excellent broadband light-harvesting capacity (λ_{max} = 537 nm) due to the superior UV and visible-light harvesting capacity of CdS NRs (λ_{max} = 545 nm), and the synergistic heterointerface further leads to enhanced light absorption capacity at wavelength range of $\lambda <$ 480 nm compared with CdS NRs. Alternating current (AC) impedance plots tested under light-irradiation (Fig. S4) suggests significantly reduced interfacial resistance of CdS/TiO$_{2(20\%)}$ composite photocatalyst

compared with bare TiO$_2$ NPs and CdS NRs, indicating the synergistic acceleration of photoexciton conduction at TiO$_2$/CdS heterointerface, and further resulting restrained photoexciton recombination. Photoinduced transient linear sweep voltammetry (LSV) curves in Fig. 4(g) show that the CdS/TiO$_{2(20\%)}$ composite photocatalyst appears significantly enhanced photocurrent signals in a wide initial potential range of −0.8–0 V compared with TiO$_2$ NPs and CdS NRs, and subsequent transient photocurrent-time curves in Fig. 4(h) also show the similar result. On the one hand, excellent light-harvesting capacity of CdS/TiO$_{2(20\%)}$ composite photocatalyst greatly promotes the electron-hole separation under broadband light-irradiation. On the other hand, accelerated interfacial photoexciton conduction dynamics effectively increases the utilization efficiency of photoexcitons due to the restrained recombination dynamics.

Band structure of photocatalyst determines the dynamics of exciton generation and transfer after photoactivation. Both Mott-Schottky curves of TiO$_2$ NPs (Fig. 4(i)) and CdS NRs (Fig. 4(j)), measured at different frequencies (1000, 1500, 2000 Hz), show positive slope in linear parts, which corresponds to n-type semiconductor feature [40]. Moreover, flat band potential (E$_{fb}$) can be determined to be −2.13 V

(TiO₂) and −1.43 V (CdS) *vs.* Ag⁺/AgCl electrode, which can be converted to −1.52 V (TiO₂) and −0.82 V (CdS) *vs.* reversible hydrogen electrode (RHE) by following the method in literature [30]. Therefore, conduction band potential (E$_{CB}$) can be determined as −1.72 V (TiO₂) and −1.02 V (CdS) *vs.* RHE according to the method in literature [41]. Based on the (Ahν)$^{n/2}$-hν patterns in Fig. 4(f), the band gaps (E$_g$) can be determined to be 2.92 eV (TiO₂) and 2.34 eV (CdS), so valence band potentials (E$_{VB}$) can be determined to be 1.20 V (TiO₂) and 1.32 V (CdS) *vs.* RHE, and their band structures are shown as Fig. S6.

Femtosecond transient absorption (fs-TA) spectroscopy is an effective means to investigate the exciton dynamics of photocatalysts, so it was tested on 380 nm pulse pump and 450–780 nm white light pulse probe. Under excitation, both two-dimensional (2D) mapped TA spectra of CdS NRs (Fig. S5(a)) and CdS/TiO$_{2(20\%)}$ composite photocatalyst (Fig. 4(a)) show obvious excited state absorption (ESA) signal around 471 nm, which ascribes to the generation of heat excitons in CB of CdS under excitation. Moreover, ground state bleaching (GSB) signal around 510 nm ascribes to the number decrease of ground-state excitons, indicating the exciton transition to excited state after absorbing pumping pulsed laser [42]. Fig. 4(b,c) show the TA spectra of CdS/TiO$_{2(20\%)}$ composite photocatalyst at different relaxation times. After photoexcitation, the TA intensity of GSB signal shows a rapid increase trend at fs scale (Fig. 4(b)) followed by a gradual attenuation trend in the subsequent ps and ns ranges (Fig. 4(c)), which correspond to the dynamics of

photoexcitation separation and recombination of the catalyst, respectively [43]. The GSB signal of CdS/TiO$_{2(20\%)}$ composite photocatalyst shows obviously increased maximum TA intensity (ΔA = −10.01 mOD) compared with CdS NRs (ΔA = −5.84 mOD), indicating that CdS/TiO$_{2(20\%)}$ composite photocatalyst can produce higher density of photoexcitons under the same excitation condition. In addition, a negative signal at 564 nm can be observed from the 900 fs-TA spectrum (Fig. 4(b)), while CdS NRs does not present the similar characteristic (Fig. S5(b)), which ascribes to the promoted exciton separation and TiO₂-to-CdS exciton transfer at CdS/TiO₂ heterinterface [44,45]. Therefore, the band structure of CdS/TiO$_{2(20\%)}$ composite photocatalyst can be proposed as Fig. 4(k). Multi-exponential function fitting decay kinetics curve in Fig. 4(d) shows two fast processes (τ₁ = 9.3 ps and τ₂ = 95 ps) and a slow process (τ₃ = 903 ps). The τ₁ and τ₂ correspond to electron capture and transfer processes, and τ₃ corresponds to exciton recombination process. Compared with CdS NRs (τ₁ = 13 ps and τ₂ = 276 ps, Fig. S5(d)), the CdS/TiO$_{2(20\%)}$ composite photocatalyst appears a shorter τ₁ (9.3 ps), indicating the faster electron transfer from CB to capturing state, which is attributed to that the built-in electric field at CdS/TiO₂ heterointerface highly promotes the exciton separation and transfer under photoexcitation. Meanwhile, the CdS/TiO$_{2(20\%)}$ composite photocatalyst has a longer τ₃ (903 ps) than the τ₂ (276 ps) of CdS NRs, indicating that the built-in electric field at CdS/TiO₂ heterointerface greatly suppresses the exciton recombination kinetics [46].
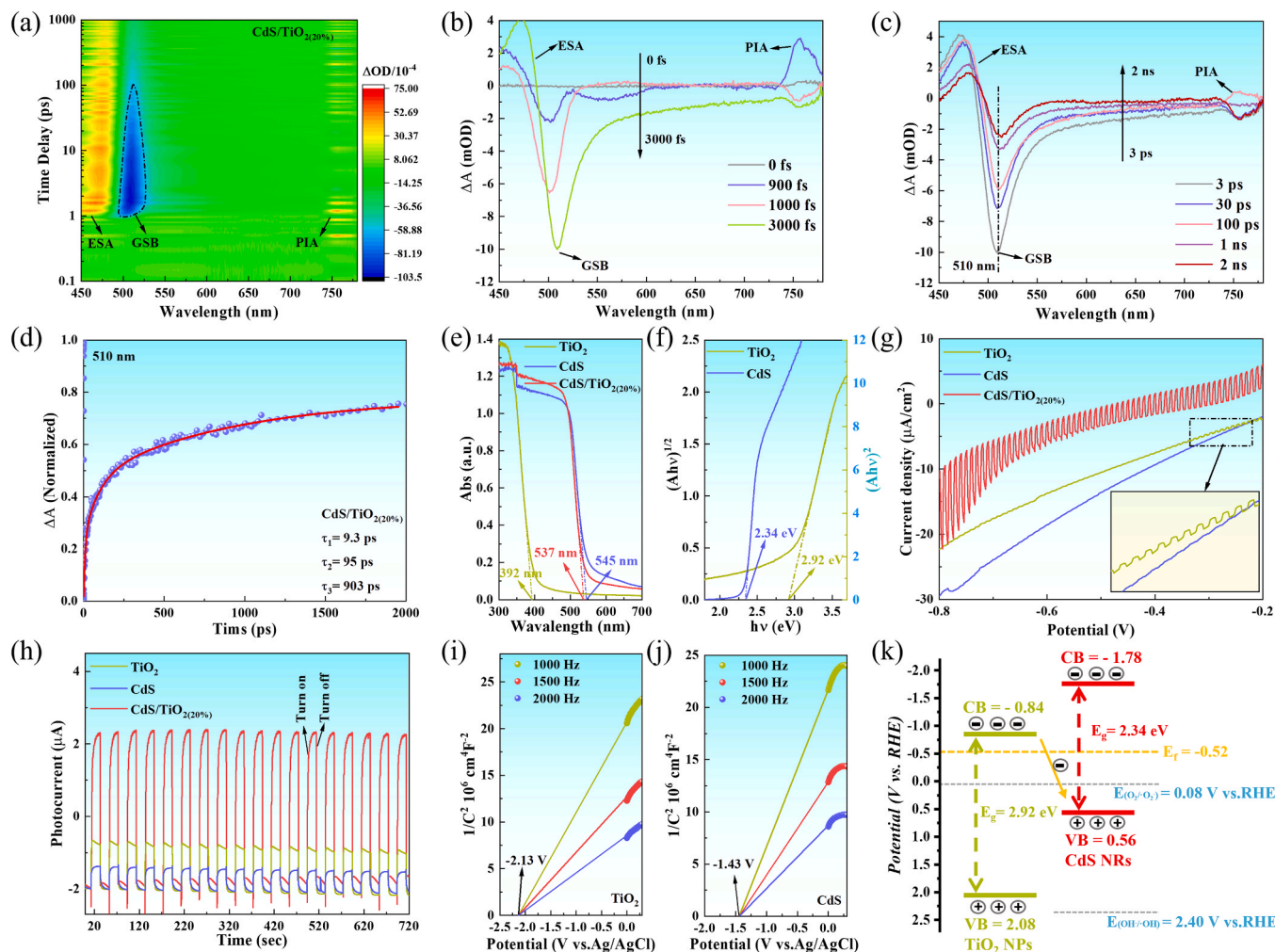

Fig. 4. (a) 2D mapped TA spectrum, (b) TA spectra, (c) attenuated TA spectra and (d) decay kinetics curve of CdS/TiO$_{2(20\%)}$ composite photocatalyst. (e) UV-Vis absorption spectra, (g) transient LSV curves and (h) transient photocurrent-time curves of TiO₂ NPs, CdS NRs and CdS/TiO$_{2(20\%)}$ composite photocatalyst. (f) (Ahν)$^{n/2}$-hν patterns and (i,j) Mott-Schottky curves of TiO₂ NPs and CdS NRs. (k) Band structure of CdS/TiO$_{2(20\%)}$ composite photocatalyst. fs-TA tests were performed under excitation of a 380 nm-pump pulse. Transient photocurrent-time curves in panel (h) were tested in an initial potential of −0.2 V.

3.4. Membrane catalyst and its comprehensive performance

In order to improve the operability and structural stability of inorganic particulate catalyst for meeting the standard of practical application, optimized CdS/TiO_2 composite photocatalyst was uniformly mixed with PVDF powder in mixed liquor of acetone and dimethyl formamide (DMF) to process into a membrane structure shown as Fig. 1 and Fig. 6(a) via an electrospinning technique. SEM image in Fig. 5(a) shows that pristine PVDF membrane is composed of interwoven microfibers with smooth surface. After compounding $CdS/TiO_{2(20\%)}$ composite photocatalyst, the fiber surface becomes rough and uneven with expose of a large number of particles. With amount increase of inorganic catalyst (Fig. 5(b-f)), the number of exposed particles increases correspondingly, thereby the exposed particles can be determined to be $CdS/TiO_{2(20\%)}$ composite photocatalyst. Moreover, Fourier transform infrared (FTIR) spectra in Fig. 5(h) shows that PVDF/CT membranes still display the similar α, β, γ phases compared with pure PVDF membrane, indicating that the compound of inorganic catalyst did
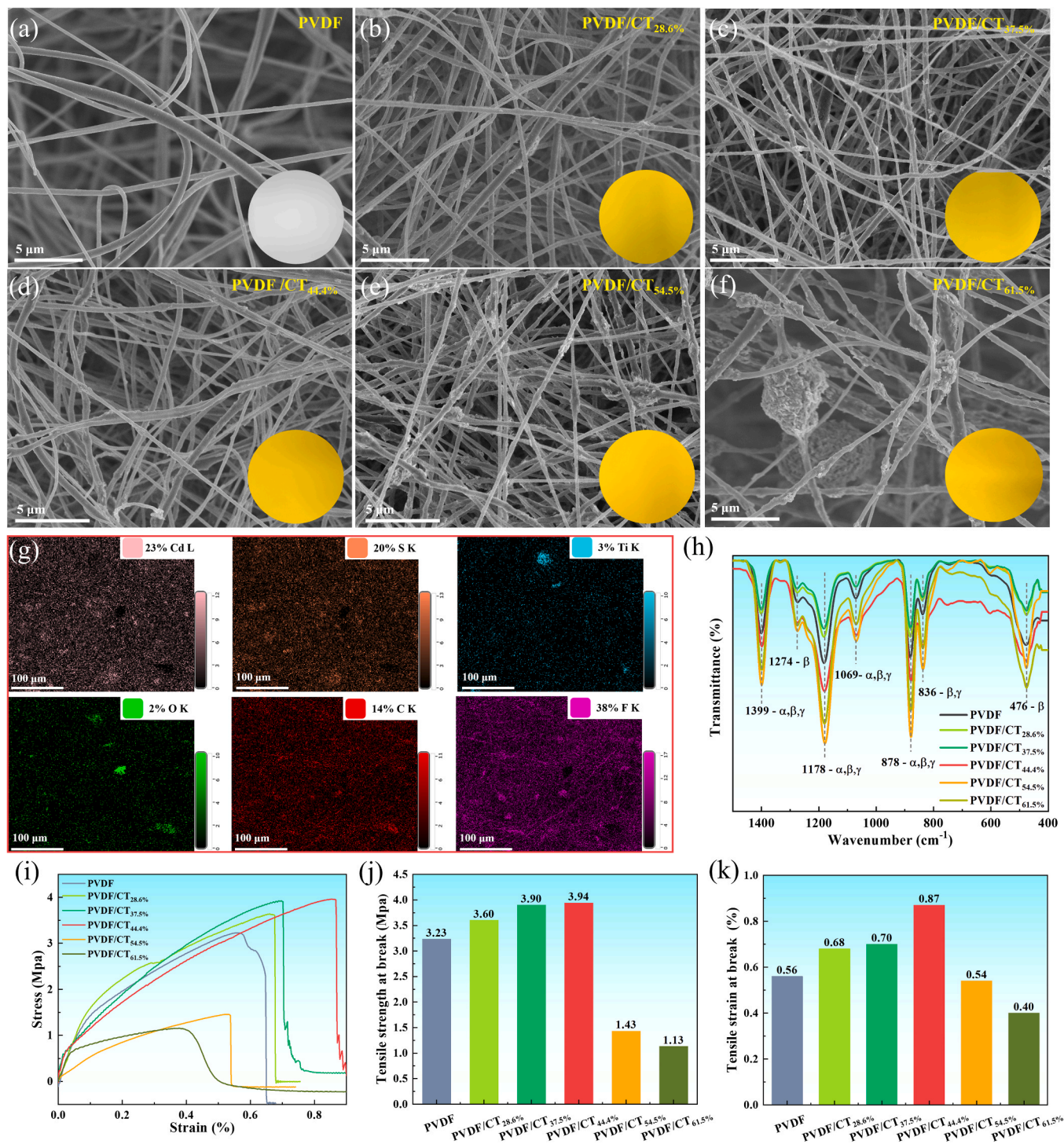

Fig. 5. (a-f) SEM images, (h) FTIR spectra, (i) stress-strain curves, (j) tensile strengths and (k) tensile elongation yields of PVDF membrane and PVDF/CT membrane catalysts with different amounts of inorganic catalyst (28.6%, 37.5%, 44.4%, 54.5% and 61.5%). (g) EDS mappings of PVDF/CT$_{54.5\%}$ membrane catalyst. Insets of panels (a-f) are the corresponding digital photos of membrane catalysts.

not influence the ferroelectric structure of PVDF matrix. Meanwhile, with addition of inorganic catalyst, both the tensile strength and tensile elongation yield of membrane materials show a trend of increasing first and then decreasing (Fig. 5(i-k)), which indicates that compounding appropriate amount of inorganic catalyst benefits to the formation of strong interaction at organic-inorganic interface following an improved mechanical strength. When using a circular membrane catalyst with a diameter of 10 cm to replace inorganic catalyst to promote CTC reduction under SSL-irradiation (Fig. 6(b,c)), pure PVDF membrane shows a very poor CTC reduction capacity, while all composite membranes appear remarkable CTC reduction capacity. In particular, the PVDF/CT$_{54.5\%}$ membrane catalyst shows the highest CTC reduction rate (0.016 min^{-1}) due to appropriate addition of inorganic catalyst, and

Cr^{6+} ions in aqueous solution was completely reduced to Cr^{3+} ions during 4 h of irradiation. In contrast, both few and excessive addition of inorganic catalyst result in decreased CTC reduction capacity of PVDF/CT membrane catalyst. On the one hand, lower amount of inorganic catalyst in composite membrane makes less expose of effective active sites, leading to lower reaction frequency. On the other hand, excessive inorganic catalyst in composite membrane leads to obvious particulate aggregation in PVDF matrix (Fig. 5(f)), which is not conducive to the expose of effective active sites and the formation of synergistic organic-inorganic interface. X-ray energy dispersive spectrometer (EDS) mappings of PVDF/CT$_{54.5\%}$ membrane catalyst show uniform distributions of each element (Fig. 5(g)), suggesting that appropriate amount of inorganic catalyst benefits to its good dispersion in organic PVDF matrix,
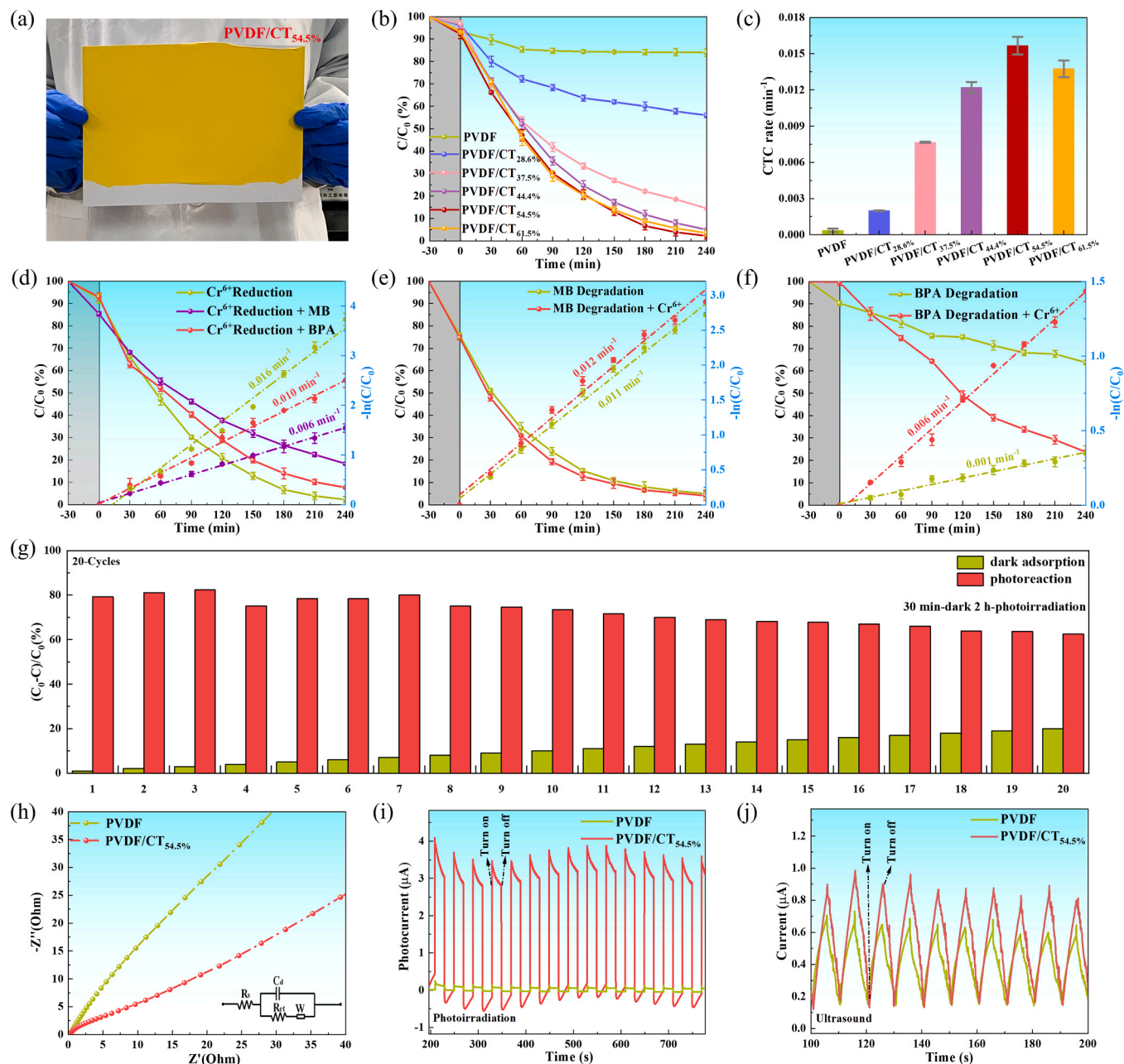

Fig. 6. (a) Digital photo of PVDF/CT$_{54.5\%}$ membrane catalyst. (b,c) CTC reduction performances of PVDF/CT membrane catalysts with different amount of CdS/TiO$_2$ $_{(20\%)}$ composite catalyst. (d) Cr^{6+}, (e) MB and (f) BPA treating performances of mixed solution containing 0.4 mM Cr^{6+} and 10 mg/L MB or BPA by PVDF/CT$_{54.5\%}$ membrane catalyst. (g) Cyclic CTC reduction performance of PVDF/CT$_{54.5\%}$ membrane catalyst. (h) AC impedance plots, (i) transient photocurrent-time curves and (j) transient piezoelectric current-time curves of pure PVDF membrane and PVDF/CT$_{54.5\%}$ membrane catalyst. Error bars of panels (b-f) were determined through three measurements.

thereby high photoactivity can be obtained. More importantly, the PVDF/CT$_{54.5\%}$ membrane catalyst still maintains outstanding CTC reduction capacity even being used for 20 cycles, suggesting superior photostability. The SEM image of the recovered PVDF/CT$_{54.5\%}$ membrane catalyst shows unconspicuous variation in its fibrous structure except the slightly increased fiber space (Fig. S7), which provides the evidence for above conclusion.

In order to further assess the comprehensive CCW purification performance of optimized membrane catalyst, both 0.4 mM Cr^{6+} and 10 mg/L MB or BPA were used as targeted contaminants to add into water phase. As shown in Fig. 6(d), the fabric structure of membrane material is greatly conducive to the capture of organic matters in aqueous phase, and about 95% of MB (1.1×10^{-2} min^{-1}) or 36.2% of BPA (0.1×10^{-2} min^{-1}) was degraded during 4 h of SSL-irradiation. Comparatively, when Cr^{6+} co-exists in aqueous phase, this membrane catalyst showed further enhanced degradation activity, and about 96% of MB (1.2×10^{-2} min^{-1}) or 76.3% of BPA (0.6×10^{-2} min^{-1}) was degraded during 4 h of SSL-irradiation (Fig. 6(e,f)), which is benefited from that the CTC reduction half-reaction effectively suppresses the exciton recombination kinetics and greatly promotes the oxidation half-reaction. Notably, mixed solution showed a reduced CTC reduction capacity to a certain extent compared with that of single Cr^{6+} solution, which attributes to the consuming of a small amount of reducing excitons (e$^-$) in degradation process of organic matters.
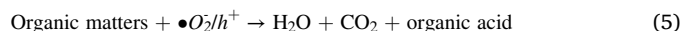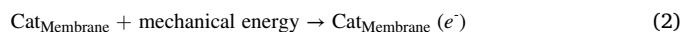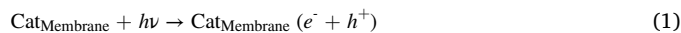
AC impedance plots in Fig. 6(h) show that the compound of inorganic catalyst significantly reduces the interfacial impedance of PVDF matrix, which ascribes to the synergistic promotion of CdS/TiO$_2$ heterointerface and organic-inorganic interface, and is more conducive to the exciton conduction. As shown as transient photocurrent-time curves in Fig. 6(i), pure PVDF membrane appears poor photocurrent response under transient photoirradiation, while PVDF/CT$_{54.5\%}$ membrane catalyst shows remarkably enhanced photocurrent response under same photoirradiation, indicating that the compound of inorganic catalyst significantly promotes the exciton separation of membrane material, which is attributed to the superior broadband light harvesting capacity of inorganic catalyst (Fig. 4(e)) and synergistic effect of organic-inorganic interface. Moreover, as shown in Fig. 6(j), this membrane catalyst also appears a strong response current signals under 40 kHz of ultrasound induction, which proves the piezoelectronic property of ferroelectric PVDF matrix. Compared with pure PVDF membrane, the piezoelectric current intensity is highly increased, which indicates that the synergistic effect of organic-inorganic interface greatly benefits to enhance the piezoelectric property of membrane material. Therefore, the PVDF/CT$_{54.5\%}$ membrane catalyst is confirmed to have the potential of multi-field-driven catalysis under inductions of light energy and mechanical energy, and the corresponding piezoelectric-voltage and piezoelectric-current tests in Fig. S8 support this conclusion well.

3.5. Panel purification system for CCW

Based on above highly active and steady membrane catalyst, a novel panel wastewater purification system shown as Fig. 7(a) was first built, which was consisted of two panel reaction modules filled with membrane catalyst (23 cm×16 cm), a liquid exchange bottle (300 mL), a peristaltic pump and two xenon lamps (300 W). Under the drive of peristaltic pump, 2.2 L of prepared mixed aqueous solution containing 0.4 mM Cr^{6+} and 10 mg/L MB was injected into the panel reaction modules at a flow rate of 60 mL/min through liquid exchange bottle. In this process, rapid color variation of membrane catalyst from original yellow to green was observed as Fig. 7(b), which ascribes to the strong adsorption resulting from the good surface affinity of organic-inorganic matrix to MB molecules in aqueous solution. As shown in Fig. 7(c), after 30 min of circulation of mixed solution in panel system, both MB and calibrated Cr^{6+} ions in mixed solution showed decreased absorption peak intensity, and 8.7% of MB and 8.8% of Cr^{6+} ions were adsorbed by membrane catalyst, respectively. Subsequently, xenon lamps were used

to irradiate the panel reaction modules, and the solution was extracted for detection every 1 h. As shown in Fig. 7(c), with extension of illumination time, the absorption peak intensity of two targeted pollutants gradually decreased until it completely disappeared after 8 h. The insets of Fig. 7(c,d) show that the colors of two targeted pollutants gradually weakened and became completely colorless during this process. Meanwhile, kinetic curves in Fig. 7(d) show that the contents of MB and Cr^{6+} ions gradually decreased to zero during 8 h of photoirradiation, and the corresponding degradation and reduction rates were 7.50×10^{-3} min^{-1} and 8.83×10^{-3} min^{-1}, respectively. Notably, after the reaction, the membrane catalyst in panel reaction modules returned to the original yellow color from green color (Fig. 7(b)), which provides powerful evidence for complete CTC reduction and synchronous degradation of organic matters.

According to above exciton dynamics and band structure of the catalyst, purifying mechanism of targeted pollutants can be determined as Fig. 7(e). Inorganic CdS/TiO$_{2(20\%)}$ composite catalyst can be activated to produce heat excitons (e$^-$ and h$^+$) accompanied by generation of •O$_2^-$ radicals under photoirradiation. Meanwhile, under the action of fluid shear stress, a large number of polarized electrons can be produced in PVDF matrix due to its piezoelectron polarization, which subsequently transfer to the active sites of CdS/TiO$_{2(20\%)}$ composite catalyst. Therefore, Cr^{6+} ions and organic matters can quickly capture the reducing excitons (e$^-$) and oxidizing excitons (•O$_2^-$ and h$^+$) from the surface of membrane catalyst to be rapidly reduced and decomposed to achieve the complete CCW purification. The specific processes are shown as follows:

$$\text{Cat}_{Membrane} + h\nu \rightarrow \text{Cat}_{Membrane}\ (e^- + h^+) \tag{1}$$

$$\text{Cat}_{Membrane} + \text{mechanical energy} \rightarrow \text{Cat}_{Membrane}\ (e^-) \tag{2}$$

$$O_2 + e^- \rightarrow \bullet O_2^- \tag{3}$$

$$Cr^{6+} + e^- \rightarrow Cr^{3+} \tag{4}$$

$$\text{Organic matters} + \bullet O_2^-/h^+ \rightarrow H_2O + CO_2 + \text{organic acid} \tag{5}$$

4. Conclusion

In summary, a synergistically electronic interacted membrane catalyst with large extending area and high pollutant capture capacity was processed based on a highly active CdS/TiO$_2$ heterojunction and ferroelectric PVDF for achieving highly efficient CTC reduction (1.6×10^{-2} min^{-1}) and synchronous decomposition of organic matters (MB (1.2×10^{-2} min^{-1}) and BPA (0.6×10^{-2} min^{-1})) under 74.1 mW·cm^{-2} of SSL irradiation following a durably steady photoactivity even being recycled for 20 times, which effectively avoided the hazards of secondary pollution. Subsequently, a tailor-made panel wastewater purification system was built based on this membrane catalyst to progress the CTC reduction and synchronous organic matter degradation, and high-efficiency purification performance was presented on this panel system under multi-field drive of light-activation and piezoelectric polarization. This work provides an insight for photocatalytic wastewater purification through membrane catalyst assisted panel technology.

CRediT authorship contribution statement

Wei Li: Writing – review & editing, Writing – original draft, Visualization, Validation, Supervision, Software, Resources, Project administration, Methodology, Investigation, Funding acquisition, Formal analysis, Data curation, Conceptualization. **Guocheng Liao:** Writing – review & editing, Writing – original draft, Investigation, Formal analysis. **Yusen Wang:** Writing – review & editing, Investigation. **Rongxia Cui:** Writing – review & editing, Investigation. **Wen Duan:** Writing – review & editing, Investigation. **Fanfan Gao:** Writing – review &
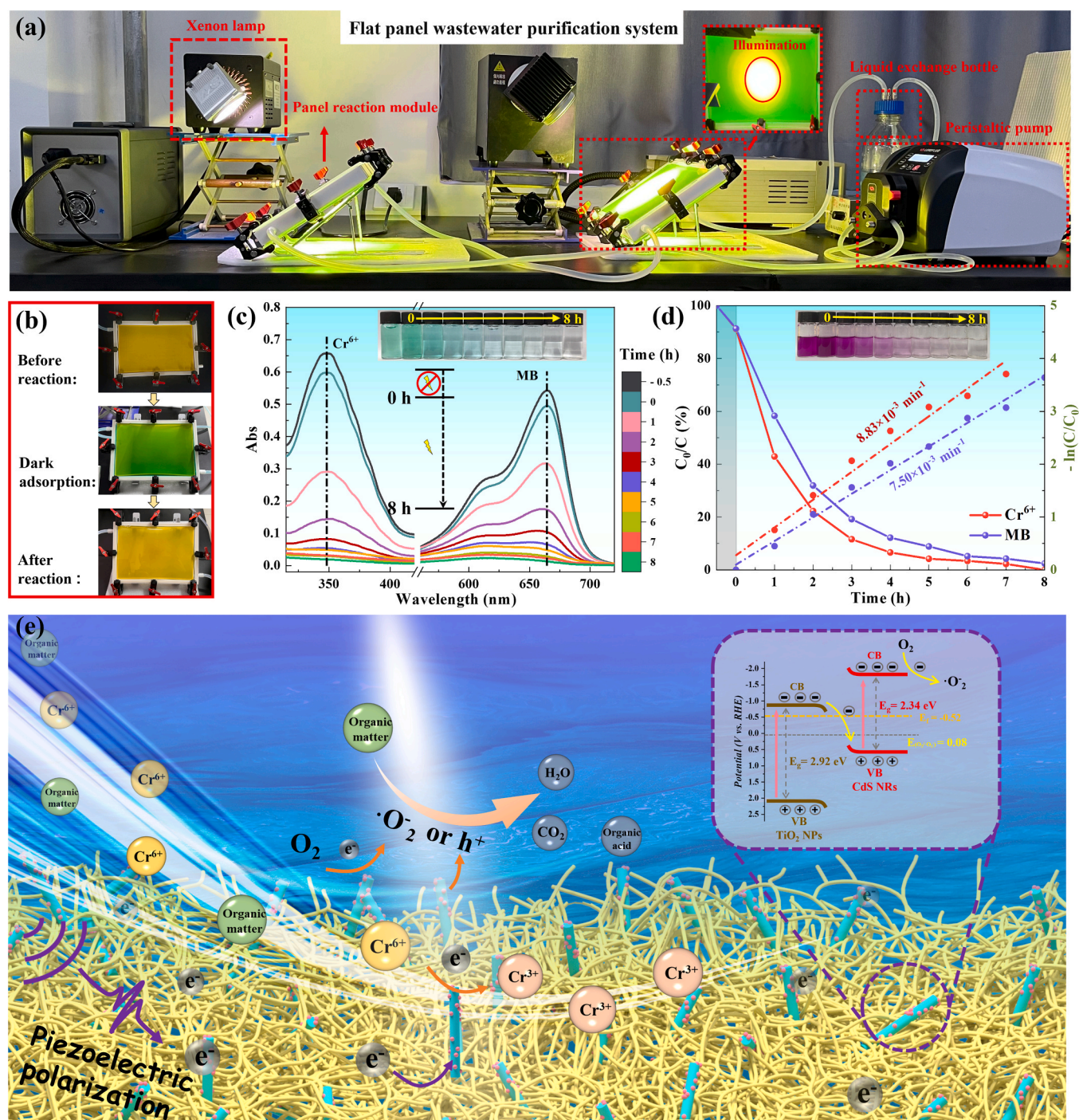
Fig. 7. (a) Panel wastewater purification system. (b) Color variation of panel reaction modules in different stages. (c) UV-Vis spectrograms and (d) corresponding purifying performances of mixed solution containing Cr^{6+} and MB in different circulation time under photoirradiation. Insets of panels (c) and (d) present the color variation of MB (blue) and calibrated Cr^{6+} ions (fuchsia) in mixed solution at different intervals. (e) Photocatalytic CCW purification mechanism of membrane catalyst. The initial concentrations of Cr^{6+} and MB in mixed solution were 0.4 mM and 10 mg/L, respectively.

editing, Investigation. **Xuechuan Wang:** Writing – review & editing, Resources, Methodology, Conceptualization. **Chuanyi Wang:** Writing – review & editing, Resources, Methodology, Funding acquisition, Data curation.

Declaration of Competing Interest

Data availability

Data will be made available on request.

Appendix A. Supporting information

Supplementary data associated with this article can be found in the online version at doi:10.1016/j.apcatb.2024.124108.

References

[1] M. Li, N. Chen, H. Shang, C. Ling, K. Wei, S. Zhao, B. Zhou, F. Jia, Z. Ai, L. Zhang, An electrochemical strategy for simultaneous heavy metal complexes wastewater treatment and resource recovery, *Environ. Sci. Technol.* 56 (2022) 10945–10953.

[2] G. Dong, B. Chen, B. Liu, L.J. Hounjet, Y. Cao, S.R. Stoyanov, M. Yang, B. Zhang, Advanced oxidation processes in microreactors for water and wastewater treatment: development, challenges, and opportunities, Water Res. 211 (2022) 118047.

[3] G. Hu, C. Long, L. Hu, Y. Zhang, S. Hong, Q. Zhang, P. Zheng, Z. Su, J. Xu, L. Wang, X. Gao, X. Zhu, F. Yuan, T. Wang, S. Yu, G. Jia, Blood chromium exposure, immune inflammation and genetic damage: exploring associations and mediation effects in chromate exposed population, J. Hazard. Mater. 425 (2022) 127769.

[4] D. Lei, C. Gou, C. Wang, J. Xue, Z. Zhang, W. Liu, Z. Lin, J. Zhang, Visible light accelerates Cr(III) release and oxidation in Cr-Fe chromite residues: an overlooked risk of Cr(VI) reoccurrence, Environ. Sci. Technol. 56 (2022) 17674–17683.

[5] G. Zhou, Q. Wu, L. Wu, L. Liu, D. Wang, P. Wang, Reaction kinetic acceleration induced by atomic-hybridized channels in carbon quantum dot/ReS2 composites for efficient Cr(VI) reduction, Appl. Catal. B-Environ. 300 (2022) 119807.

[6] B.-M. Kim, B. Kim, S.-E. Nam, H.-J. Eom, S. Lee, K. Kim, J.-S. Rhee, Reductive transformation of hexavalent chromium in ice decreases chromium toxicity in aquatic animals, Environ. Sci. Technol. 56 (2022) 3503–3513.

[7] Z. Zhu, J. Li, W. Li, X. Liu, Y. Dang, T. Ma, C. Wang, Simulated-sunlight-driven Cr (VI) reduction on type-II heterostructured Sb2S3/CdS photocatalyst, Environ. Sci.: Nano 9 (2022) 1738–1747.

[8] W. Li, J. Li, T. Ma, G. Liao, F. Gao, W. Duan, K. Luo, C. Wang, Construction of core-chell Sb2S3@CdS nanorod with enhanced heterointerface interaction for chromium-containing wastewater treatment, Small 19 (2023) 2302737.

[9] S. Zhang, C. Li, C. Ke, S. Liu, Q. Yao, W. Huang, Z. Dang, C. Guo, Extracellular polymeric substances sustain photoreduction of Cr(VI) by Shewanella oneidensis-CdS biohybrid system, Water Res. 243 (2023) 120339.

[10] G.Z.S. Ling, S-F. Ng, W.-J. Ong, Tailor-engineered 2D cocatalysts: Harnessing electron-hole redox center of 2D g-C3N4 photocatalysts toward solar-to-chemical conversion and environmental purification, Adv. Funct. Mater. 32 (2022) 2111875.

[11] B. Ran, L. Ran, Z. Wang, J. Liao, D. Li, K. Chen, W. Cai, J. Hou, X. Peng, Photocatalytic antimicrobials: principles, design strategies, and applications, Chem. Rev. 123 (2023) 12371–12430.

[12] J. Chakraborty, I. Nath, F. Verpoort, A physicochemical introspection of porous organic polymer photocatalysts for wastewater treatment, Chem. Soc. Rev. 51 (2022) 1124–1138.

[13] Q. Zhang, J. Chen, X. Gao, H. Che, P. Wang, Y. Ao, In-depth insight into the mechanism on photocatalytic synergistic removal of antibiotics and Cr (VI): the decisive effect of antibiotic molecular structure, Appl. Catal. B-Environ. 313 (2022) 121443.

[14] T. Xue, L. Chen, K. Li, B. Lei, H. Wang, F. Dong, Y. Yang, Highly enhanced photocatalytic NO removal and inhibited peroxyacetyl nitrate formation in synergistic acetaldehyde degradation, Environ. Sci. Technol. 57 (2023) 8174–8182.

[15] Y. Yuan, L. Zhou, H. Robatjazi, J.L. Bao, J. Zhou, A. Bayles, L. Yuan, M. Lou, M. Lou, S. Khatiwada, E.A. Carter, P. Nordlander, N.J. Halas, Earth-abundant photocatalyst for H2 generation from NH3 with light-emitting diode illumination, Science 378 (2022) 889–893.

[16] R. Chen, Z. Ren, Y. Liang, G. Zhang, T. Dittrich, R. Liu, Y. Liu, Y. Zhao, S. Pang, H. An, C. Ni, P. Zhou, K. Han, F. Fan, C. Li, Spatiotemporal imaging of charge transfer in photocatalyst particles, Nature 610 (2022) 296–301.

[17] Z. Li, R. Li, H. Jing, J. Xiao, H. Xie, F. Hong, N. Ta, X. Zhang, J. Zhu, C. Li, Blocking the reverse reactions of overall water splitting on a Rh/GaN-ZnO photocatalyst modified with Al2O3, Nat. Catal. 6 (2023) 80–88.

[18] S. Mukherjee, L. Zhou, A.M. Goodman, N. Large, C. Ayala-Orozco, Y. Zhang, P. Nordlander, N.J. Halas, Hot-electron-induced dissociation of H2 on gold nanoparticles supported on SiO2, J. Am. Chem. Soc. 136 (2014) 64–67.

[19] Y. Wei, P. Zhang, J. Xiong, Q. Yu, Q. Wu, Z. Zhao, J. Liu, SO2-tolerant catalytic removal of soot particles over 3D ordered macroporous Al2O3-supported binary Pt-Co oxide catalysts, Environ. Sci. Technol. 54 (2020) 6947–6956.

[20] Y. Zhou, X. Zhang, G. Sheng, S. Wang, M. Chen, G. Zhuang, Y. Zhu, P. Du, A metal-free photoactive nitrogen-doped carbon nanosolenoid with broad absorption in visible region for efficient photocatalysis, Nat. Commun. 14 (2023) 5831.

[21] H. Nishiyama, T. Yamada, M. Nakabayashi, Y. Maehara, M. Yamaguchi, Y. Kuromiya, Y. Nagatsuma, H. Tokudome, S. Akiyama, T. Watanabe, R. Narushima, S. Okunaka, N. Shibata, T. Takata, T. Hisatomi, K. Domen, Photocatalytic solar hydrogen production from water on a 100-m² scale, Nature 598 (2021) 304–307.

[22] P. Zhou, I.A. Navid, Y. Ma, Y. Xiao, P. Wang, Z. Ye, B. Zhou, K. Sun, Zetian Mi, Solar-to-hydrogen efficiency of more than 9% in photocatalytic water splitting, Nature 613 (2023) 66–70.

[23] W. Li, Q. Ma, X. Wang, X. Chu, F. Wang, X. Wang, C. Wang, Enhanced photoresponse and fast charge transfer: three-dimensional macroporous g-C3N4/GO-TiO2 nanostructure for hydrogen evolution, J. Mater. Chem. A 8 (2020) 19533–19543.

[24] W. Li, Y. Dang, J. Li, T. Ma, G. Liao, F. Gao, W. Duan, J. Li, X. Wang, C. Wang, Nanoconfinement dynamics and crystal plane exposure: synergistic promotion of simulated solar-driven H2O-to-H2 conversion on host (CdS)-guest (Ti single-atom) nano-photocatalyst, Chem. Eng. J. 472 (2023) 144793.

[25] C. Xian, J. He, Y. He, J. Nie, Z. Yuan, J. Sun, W.N. Martens, J. Qin, H.-Y. Zhu, Z. Zhang, High nitrile yields of aerobic ammoxidation of alcohols achieved by generating •O2 and Br• radicals over iron-modified TiO2 photocatalysts, J. Am. Chem. Soc. 144 (2022) 23321–23331.

[26] Z. Lu, G. Zhou, B. Li, Y. Xu, P. Wang, H. Yan, M. Song, C. Ma, S. Han, X. Liu, Heterotopic reaction strategy for enhancing selective reduction and synergistic oxidation ability through trapping Cr (VI) into specific reaction site: a stable and self-cleaning ion imprinted CdS/HTNW photocatalytic membrane, Appl. Catal. B-Environ. 301 (2022) 120787.

[27] Z. Chen, Y. Ye, X. Feng, Y. Wang, X. Han, Y. Zhu, S. Wu, S. Wang, W. Yang, L. Wang, J. Zhang, High-density frustrated Lewis pairs based on Lamellar Nb2O5 for photocatalytic non-oxidative methane coupling, Nat. Commun. 14 (2023) 2000.

[28] W. Li, X. Chu, F. Wang, Y. Dang, X. Liu, T. Ma, J. Li, C. Wang, Pd single-atom decorated CdS nanocatalyst for highly efficient overall water splitting under simulated solar light, Appl. Catal. B-Environ. 304 (2022) 121000.

[29] W. Li, F. Wang, X. Liu, Y. Dang, J. Li, T. Ma, C. Wang, Promoting body carriers migration of CdS nanocatalyst by N-doping for improved hydrogen production under simulated sunlight irradiation, Appl. Catal. B-Environ. 313 (2022) 121470.

[30] Z. Lu, J. Gao, S. Rao, C. Jin, H. Jiang, J. Shen, X. Yu, W. Wang, L. Wang, J. Yang, Q. Liu, A multifunctional membrane based on TiO2/PCN-224 heterojunction with synergistic photocatalytic-photothermal activity under visible-light irradiation, Appl. Catal. B-Environ. 342 (2024) 123374.

[31] X. Ma, Y. Shi, J. Liu, X. Li, X. Cui, S. Tan, J. Zhao, B. Wang, Hydrogen-bond network promotes water splitting on the TiO2 surface, J. Am. Chem. Soc. 144 (2022) 13565–13573.

[32] Y. Shen, C. Ren, L. Zheng, X. Xu, R. Long, W. Zhang, Y. Yang, Y. Zhang, Y. Yao, H. Chi, J. Wang, Q. Shen, Y. Xiong, Z. Zou, Y. Zhou, Room-temperature photosynthesis of propane from CO2 with Cu single atoms on vacancy-rich TiO2, Nat. Commun. 14 (2023) 1117.

[33] F. Cheng, J. Zhang, K. Xie, In situ observation of porosity formation in porous single-crystalline TiO2 monolith for enhanced and stable catalytic CO oxidation, Angew. Chem. Int. Ed. 62 (2022) e202300480.

[34] H. Lei, T. Li, J. Li, J. Zhu, H. Zhang, H. Qin, X. Kong, L. Wang, X. Peng, Reversible facet reconstruction of CdSe/CdS core/shell nanocrystals by facet-ligand pairing, J. Am. Chem. Soc. 145 (2023) 6798–6810.

[35] X. Zhang, F. Wu, G. Li, L. Wang, J. Huang, A. Meng, Z. Li, Modulating electronic structure and sulfur p-band center by anchoring amorphous Ni@NiSx on crystalline CdS for expediting photocatalytic H2 evolution, Appl. Catal. B-Environ. 342 (2024) 123398.

[36] S. Zhou, H. Jang, Q. Qin, L. Hou, M.G. Kim, S. Liu, X. Liu, J. Cho, Boosting hydrogen evolution reaction by phase engineering and phosphorus doping on Ru/P-TiO2, Angew. Chem. Int. Ed. 61 (2022) e202212196.

[37] H. Li, S. Wang, M. Wang, Y. Gao, J. Tang, S. Zhao, H. Chi, P. Zhang, J. Qu, F. Fan, C. Li, Enhancement of plasmon-induced photoelectrocatalytic water oxidation over Au/TiO2 with lithium intercalation, Angew. Chem. Int. Ed. 61 (2022) e202204272.

[38] T. Ma, Wei Li, J. Li, W. Duan, F. Gao, G. Liao, J. Li, C. Wang, Multisite cocatalysis: Single atomic Pt2+/Pt0 active sites synergistically improve the simulated sunlight driven H2O-to-H2 conversion performance of Sb2S3 nanorods, J. Colloid. Interf. Sci. 658 (2024) 476–486.

[39] Z. Cai, X. Hu, Z. Li, H. He, T. Li, H. Yuan, Y. Zhang, B. Tan, J. Wang, Hypercrosslinking porous polymer layers on TiO2-graphene photocatalyst: Enhanced adsorption of water pollutants for efficient degradation, Water Res 227 (2022) 119341.

[40] C. Yang, M. Wang, M. Chang, M. Yuan, W. Zhang, J. Tan, B. Ding, P. Ma, J. Lin, Heterostructural nanoadjuvant CuSe/CoSe2 for potentiating ferroptosis and photoimmunotherapy through intratumoral blocked lactate efflux, J. Am. Chem. Soc. 145 (2023) 7205–7217.

[41] W. Li, X. Wang, Q. Ma, F. Wang, X. Chu, X. Wang, C. Wang, CdS@h-BN heterointerface construction on reduced graphene oxide nanosheets for hydrogen production, Appl. Catal. B-Environ. 284 (2021) 119688.

[42] W. Wang, Y. Tao, J. Fan, Z. Yan, H. Shang, D.L. Phillips, M. Chen, G. Li, Fullerene-graphene acceptor drives ultrafast carrier dynamics for sustainable CdS photocatalytic hydrogen evolution, Adv. Funct. Mater. 32 (2022) 2201357.

[43] J. Kosco, S. Gonzalez-Carrero, C.T. Howells, T. Fei, Y. Dong, R. Sougrat, G. T. Harrison, Y. Firdaus, R. Sheelamanthula, B. Purushothaman, F. Moruzzi, W. Xu, L. Zhao, A. Basu, S.D. Wolf, T.D. Anthopoulos, J.R. Durrant, I. McCulloch, Generation of long-lived charges in organic semiconductor heterojunction nanoparticles for efficient photocatalytic hydrogen evolution, Nat. Energy 7 (2022) 340–351.

[44] C. Cheng, J. Zhang, B. Zhu, G. Liang, L. Zhang, J. Yu, Verifying the charge-transfer mechanism in S-scheme heterojunctions using femtosecond transient absorption spectroscopy, Angew. Chem. Int. Ed. 62 (2023) e202218688.

[45] X.L. Wu, S. Liu, Y. Li, M. Yan, H. Lin, J. Chen, S. Liu, S. Wang, X. Duan, Directional and ultrafast charge transfer in oxygen-vacancy-rich ZnO@single-atom cobalt core-shell junction for photo-fenton-like reaction, Angew. Chem. Int. Ed. 62 (2023) e202305639.

[46] A. Wang, M. Du, J. Ni, D. Liu, Y. Pan, X. Liang, D. Liu, J. Ma, J. Wang, W. Wang, Enhanced and synergistic catalytic activation by photoexcitation driven S-scheme heterojunction hydrogel interface electric field, Nat. Commun. 14 (2023) 6733.